nanomaterials

MDPI

Article

Highly Efficient Peroxymonosulfate Electroactivation on $Co(OH)_2$ Nanoarray Electrode for Pefloxacin Degradation

Tonghui Bao, Hui Ke, Wanjiang Li, Linke Cai and Yi Huang *

Engineering Research Center of Photoenergy Utilization for Pollution Control and Carbon Reduction, Ministry of Education, College of Chemistry, Central China Normal University, Wuhan 430079, China; thbao123@mails.ccnu.edu.cn (T.B.); jczhang@mails.ccnu.edu.cn (H.K.); lwj5596@mails.ccnu.edu.cn (W.L.); cailinke@mails.ccnu.edu.cn (L.C.)

* Correspondence: yihuang@ccnu.edu.cn

Abstract: The activation of PMS to produce active species is an attractive technique for antibiotic degradation but is restricted to the low reaction kinetics and high costs. In this work, a cobalt-based catalyst was prepared by in situ electrodeposition to enhance the electrically activated PMS process for the degradation of antibiotics. Almost 100% of pefloxacin (PFX) was removed within 10 min by employing $Co(OH)_2$ as the catalyst in the electrically activated peroxymonosulfate (PMS) process, and the reaction kinetic constant reached 0.52 min^{-1}. The redox processes of Co^{2+} and Co^{3+} in $Co(OH)_2$ catalysts were considered to be the main pathways for PMS activation, in which $^1O_2$ was the main active species. Furthermore, this strategy could also achieve excellent degradation efficiency for other organic pollutants. This study provides an effective and low-cost strategy with no secondary pollution for pollutant degradation.

Keywords: peroxymonosulfate; electrochemistry; $Co(OH)_2$; wastewater treatment; pefloxacin

Citation: Bao, T.; Ke, H.; Li, W.; Cai, L.; Huang, Y. Highly Efficient Peroxymonosulfate Electroactivation on $Co(OH)_2$ Nanoarray Electrode for Pefloxacin Degradation. *Nanomaterials* **2024**, *14*, 1312. https://doi.org/10.3390/nano14151312

Academic Editor: Ki Chang Kwon

Received: 17 July 2024
Revised: 28 July 2024
Accepted: 1 August 2024
Published: 4 August 2024

1. Introduction

Treatment of medical wastewater containing antibiotics has received worldwide attention [1,2]. Pefloxacin (PFX), a fluoroquinolone, is widely used in treating viral and bacterial infections [3–5]. However, antibiotics have been discharged into aquatic ecosystems through wastewater, animal excrement, and soil erosion, which has seriously threatened both human and ecological health [6,7]. Due to the antibacterial activity, water solubility, and stability of PFX, traditional methods such as biological processes, flocculation, adsorption, and membrane processes are inadequate or ineffective for their removal [8,9]. Therefore, it is necessary to develop new processes for efficiently removing PFX and other fluoroquinolones antibiotics.

Advanced oxidation processes (AOPs) represented by activated peroxymonosulfate (PMS) have been widely studied due to its effective treatment, broad applicability, and low environmental impact [10,11]. PMS activation produces reactive species such as hydroxyl radicals (•OH), sulfate radicals ($SO_4^{\bullet-}$), and singlet oxygen ($^1O_2$) that have exhibited high potential for the removal of persistent organic pollutants and pharmaceuticals [12,13]. The activation of PMS can be achieved by many methods, such as ultraviolet, electricity, ultrasound, heat, and external catalyst activation [14,15]. Compared to other methods, metal ion activation strategies have been widely used due to their low energy consumption, simple operation, and high efficiency [16]. Meanwhile, Co^{2+} ions are regarded as the most reactive and efficient homogeneous catalyst for the activation of PMS, and the mechanism of activation of PMS is as follows [17,18]:

$$Co^{2+} + HSO_5^- \rightarrow Co^{3+} + SO_4^{\bullet-} + OH^- \quad (1)$$

$$Co^{3+} + HSO_5^- + OH^- \rightarrow Co^{2+} + SO_5^{\bullet-} + H_2O \quad (2)$$

However, the activation of PMS based on Co^{2+} ions has the disadvantages of a high ionic demand and strong pH dependence [19]. Recently, non-homogeneous catalysts represented by transition metal oxides have attracted extensive attention due to their high catalytic activity and stable crystalline structure [11,20,21]. Unfortunately, the catalyst particles dispersed in the solution are also prone to metal ion leaching, which cause secondary contamination and biotoxicity [22].

Electrochemistry is considered an effective way to enhance catalyst performance and has been widely used in the Fenton catalytic process [23]. The electric fields can accelerate electron transfer between electron donors and acceptors, which enhances PMS activation (Equation (3)) [24].

$$HSO_5^- + e^- \rightarrow SO_4^{\bullet -} + OH^- \quad (3)$$

On this basis, the combination of electrical activation and catalyst activation is a promising method for PMS activation, which not only avoids the release of toxic metal ions but also reduces the cost of catalyst [25,26]. Meanwhile, Jing et al. prepared $NiCo_2O_4$ nanoarray electrodes on a cathode for electroactivated PMS to remove rhodamine B (100 ppm), achieving 99.7% removal efficiency within 60 min [27]. Zhang et al. prepared a $MnFe_2O_4$ electrode for electroactivated PMS to promote the degradation of bisphenol A (10 ppm), achieving 100% removal efficiency within 90 min [28]. Therefore, the combination of heterogeneous and electrochemistry activation of PMS is expected to present economical and efficient degradation of antibiotics.

Considering the excellent PMS activation performance of cobalt-based catalysts, we prepared a $Co(OH)_2$ catalyst applied to the electrocatalytic system to realize the efficient removal of antibiotics by the activation of PMS. In this study, electrodes from a $Co(OH)_2$ nanosheet array grown on Ti mesh ($Co(OH)_2$@Ti) were prepared for electrochemically activated PMS to remove PFX, and we investigated the effects of pH, PMS concentration, and voltage on the degradation of PFX in this system. Then, the types and contributions of the active species produced by PMS electroactivation were identified through electron spin resonance (ESR) and free radical quenching experiments. Finally, the mechanism of PFX degradation via the $Co(OH)_2$@Ti/electroactivated PMS ($Co(OH)_2$@Ti/EA-PMS) process was proposed.

2. Materials and Methods

2.1. Preparation of $Co(OH)_2$@Ti Nanoarray Electrode

The materials and chemicals utilized are shown in the Supporting Information of Table S1. The $Co(OH)_2$@Ti nanoarray electrodes were prepared by electrochemical in situ deposition. Ti mesh (2 cm × 2 cm) was used as the working electrode, a Pt sheet was used as the counter electrode, and 0.025 mol/L cobalt nitrate ($Co(NO_3)_2$) was the electrode solution, which were reacted at −1.0 V (vs. Ag/AgCl) for 240 s. After the reaction, the Ti mesh was repeatedly cleaned and dried to obtain the $Co(OH)_2$@Ti nanoarray electrodes.

2.2. Experimental Setups

The $Co(OH)_2$@Ti/EA-PMS process was carried out using a standard three-electrode electrochemical cell, with the $Co(OH)_2$@Ti as the working electrode, Ag/AgCl as the reference electrode, and Pt mesh as the counter electrode. In the experiment of removing PFX by activating PMS, 30 mL of the mixed solutions (0.1 mol/L K_2SO_4, 10 ppm PFX) was first added to the electrolytic cell. Then, a specific amount of PMS was introduced, and an electrochemical reaction was initiated by applying a constant voltage. Meanwhile, argon gas was continuously introduced into the solution during the reaction. Each electrochemical test was performed in triplicate.

2.3. Analytical Methods

The catalyst was characterized and analyzed through scanning electron microscopy (SEM, JSM-7610E, JEOL, Tokyo, Japan), transmission electron microscopy (TEM, JEM 2100F, JEOL, Tokyo, Japan), energy-dispersive X-ray spectroscopy (EDS, Oxford, UK),

X-ray diffraction (XRD, Rigaku Ultima IV, Bruker, Saarbrucken, Germany), and X-ray photoelectron spectroscopy (XPS, K-Alpha, Thermo Scientific Waltham, MA, USA). The linear sweep voltammetry (LSV) test was carried out with a CHI 760E (Shanghai Chenhua Instrument Company, Shanghai, China). The PFX, RhB, and TC concentrations were determined by using an ultraviolet–visible spectrophotometer (UV-5500PC, Shimadzu, Kyoto, Japan), and the standard curves are shown in Figure S1. The electron spin resonance (ESR, A300, Bruker, Saarbrucken, Germany) was employed with DMPO and TEMP as spin-trapping agents for the detection of reactive species during the activation of PMS.

The PFX degradation efficiency and the pseudo-first-order rate constant were calculated using Equations (1) and (2).

$$\text{Degradation efficiency } (\%) = \frac{C_0 - C_t}{C_0} \times 100\% \quad (4)$$

$$\frac{C_t}{C_0} = exp(-kt) \quad (5)$$

where C_0 and C_t are the concentrations of PFX at 0 min and t min, respectively; and k (min^{-1}) is the pseudo-first-order rate constant.

3. Discussion

3.1. Characterization of Catalytic Electrodes

The morphology of the $Co(OH)_2$@Ti electrode surface was first evaluated through SEM analysis. As shown in Figure 1a, b, the Ti mesh surface formed a uniformly distributed petal-like structure, which provided more active sites. Correspondingly, the elemental mapping images of $Co(OH)_2$@Ti in Figure 1c confirm the uniform distribution of Co and O elements on the Ti mesh. Subsequently, the high-resolution TEM image of the $Co(OH)_2$ catalysts was obtained (Figure 1d), revealing the nanoflake micromorphology of the catalysts, which was consistent with the SEM images.

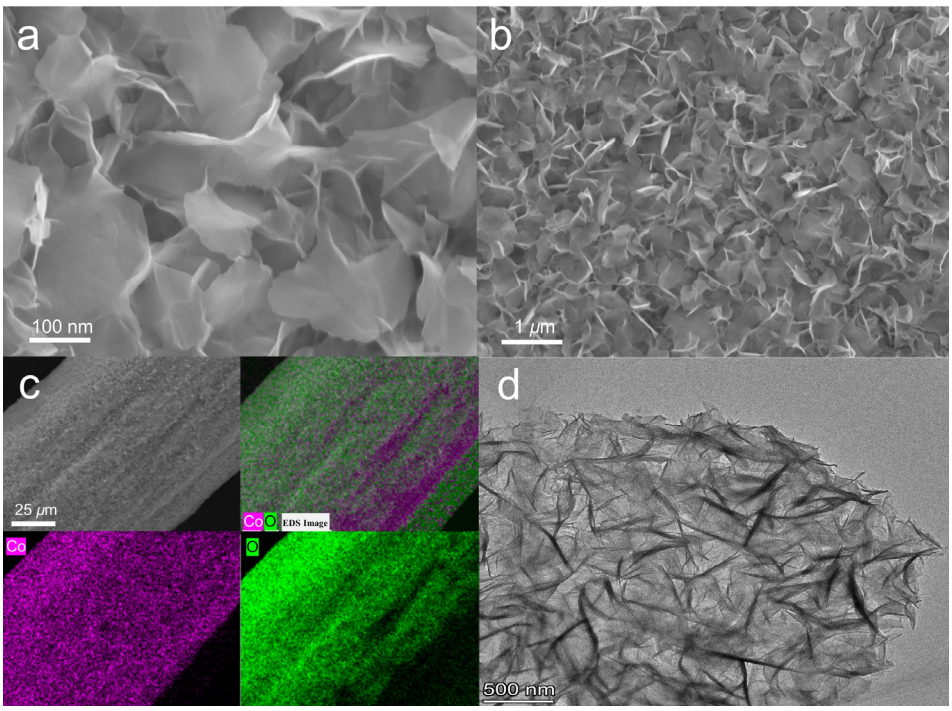

Figure 1. Morphological characterization of $Co(OH)_2$@Ti nanoarray electrodes: (**a**,**b**) SEM images at different magnifications. (**c**) EDS images and (**d**) TEM images.

XRD analysis was performed to examine the composition and structure of the $Co(OH)_2$. Meanwhile, the $Co(OH)_2$ catalysts were collected on carbon paper to avoid interference from the Ti substrate. As shown in Figure S2a, the corresponding diffraction peak corresponding to the plane of the C substrate can be found at 26.5° and 54.5°, and distinct diffraction peaks at 19.0°, 32.4°, 37.8°, 51.3°, and 57.7° are observed, which closely correspond to $Co(OH)_2$ (PDF#03-0913) [29]. The Raman spectrum displays that the peaks related to $Co(OH)_2$ appear at 665, 506, and 463 cm^{-1} (Figure S2b). Notably, no impurity peaks appear in the XRD and Raman spectra, providing evidence of the successful deposition of a pure $Co(OH)_2$ catalytic layer.

3.2. Degradation of PFX in $Co(OH)_2$@Ti/EA-PMS Process

Firstly, the PMS activation performance of the $Co(OH)_2$@Ti electrode was tested in 0.1 M K_2SO_4 with and without 200 ppm PMS electrolyte. In comparison to the scenario without PMS, the LSV curves show that the $Co(OH)_2$ catalysts demonstrate a remarkable increase in current density in the presence of PMS (Figure 2a). Furthermore, the time–current curve of PMS activated by $Co(OH)_2$ at the potential of −0.8 V (V vs. Ag/AgCl) was obtained, and the electrode solution was initially 0.1 M K_2SO_4, and 200 ppm PMS was added at 200 s (Figure 2b). Clearly, the current density increased rapidly with the addition of PMS. The above results jointly suggest the efficient electron transfer between $Co(OH)_2$ and PMS, indicating the exciting potential of $Co(OH)_2$ catalysts for PMS electroactivation.

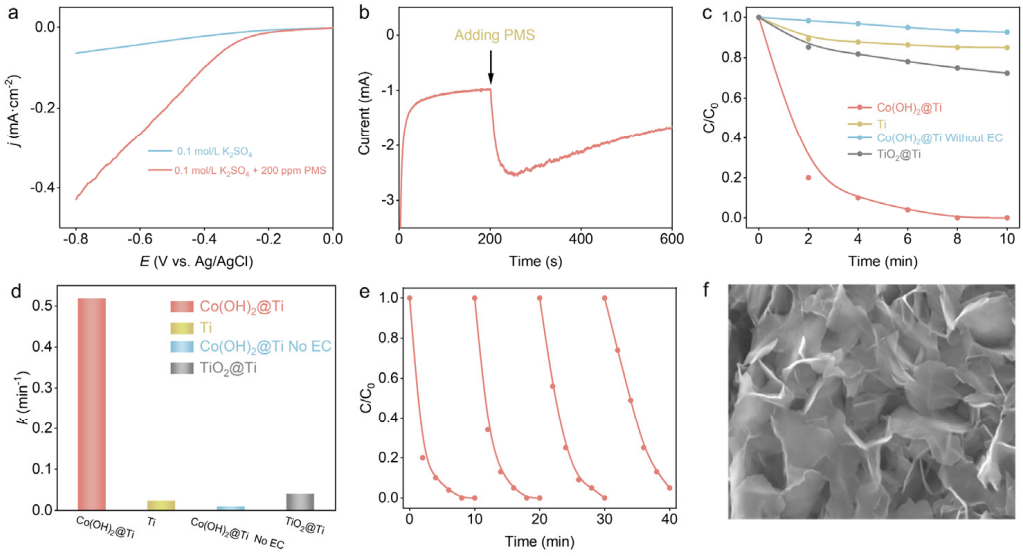

Figure 2. PFX removal performance and catalyst stability in $Co(OH)_2$@Ti/EA-PMS process. (**a**) LSV curve in $Co(OH)_2$@Ti/EA-PMS process. (**b**) Time–current curve at −0.8 V (V vs. Ag/AgCl) in $Co(OH)_2$@Ti/EA-PMS process. (**c**) Removal efficiency and (**d**) first-order kinetic fitting constants of PFX for 10 min under different reaction conditions and systems. (**e**) Reusability of $Co(OH)_2$ in $Co(OH)_2$@Ti/EA-PMS system. (**f**) SEM images of $Co(OH)_2$@Ti electrode after four-cycle experiments.

To assess the catalytic performance of the $Co(OH)_2$@Ti electrode, PFX was selected as a target pollutant. The degradation rate of PFX over time is presented in Figure 2c, with an initial concentration of 10 mg L^{-1}. The $Co(OH)_2$@Ti/EA-PMS process achieved complete removal of PFX within 10 min. In contrast, only 27.6% and 35.0% of PFX was degraded via the Ti/EA-PMS process and the TiO_2@Ti/EA-PMS process, respectively. Additionally, cobalt-based catalysts activate PMS poorly in the absence of electroactivation. Employing pseudo-first-order reaction kinetics (Figure 2d), the reaction rate constant on the $Co(OH)_2$@Ti electrode was determined to be 0.52 min^{-1}, which was significantly higher than that on the Ti electrode (0.04 min^{-1}) and the TiO_2@Ti electrode (0.02 min^{-1}). Meanwhile, the $Co(OH)_2$@Ti electrode exhibited excellent PMS activation potential, achieving 90%

activation of the PMS within 10 min (Figure S3). These results verify that the $Co(OH)_2$@Ti electrode has an inspiring potential for the removal of PFX by activating PMS. Compared to other catalytic systems, the $Co(OH)_2$@Ti/EA-PMS process not only efficiently removes organic pollutants but also significantly reduces catalyst costs (Table S2). Furthermore, the reusability of $Co(OH)_2$ in the $Co(OH)_2$@Ti/EA-PMS system was evaluated by four-cycle experiments. The PFX degradation efficiency under four consecutive reactions was 100%, 100%, 100%, and 95% (Figure 2e). The slight decrease in the catalytic activity of $Co(OH)_2$ may be attributed to the adsorption of intermediate products of PMS activation and PFX degradation on the surface of the catalysts to cover the active sites [30,31]. After four consecutive cycles, the $Co(OH)_2$ catalysts maintained their nanoflake morphology, with almost no leaching of cobalt ions (determined by inductively coupled plasma mass spectrometry (ICP-MS)) from the electrode, indicating that the catalysts have inspiring cycling stability (Figure 2f).

In order to obtain the optimal experimental conditions (e.g., pH value, PMS concentration, and voltage) of $Co(OH)_2$@Ti electroactivated PMS for the degradation of PFX, the impact of different PMS concentrations on the degradation of PFX in the $Co(OH)_2$@Ti/EA-PMS system was first investigated (Figure 3a). As the concentration of PMS increased, the degradation rate of PFX increased due to the fact that the higher concentration of PMS produced more activated radicals (Figure 3b). Figure 3c shows the effect of different potentials (−0.8 V, −1.0 V, and −1.2 V (V vs. Ag/AgCl)) on the degradation of PFX. The degradation rate of PFX increased with the increase in voltage from −0.8 V to 1.2 V due to the applied voltage increase accelerating the activation of PMS, thus accelerating the PFX degradation efficiency (Figure 3d). Furthermore, the effects of different initial pH values (4, 7, and 10) on the degradation efficiency of PFX in the $Co(OH)_2$@Ti/EA-PMS system were studied (Figures 3e and 4f). When the initial pH value was 10, the degradation rate of PFX was the best, and the PFX degradation rate constant was 0.62 min^{-1}, indicating that the weak alkaline environment was conducive to the degradation of PFX. It is noteworthy that PFX was also effectively degraded under weak acid and neutral conditions, confirming the wide pH range of the system.

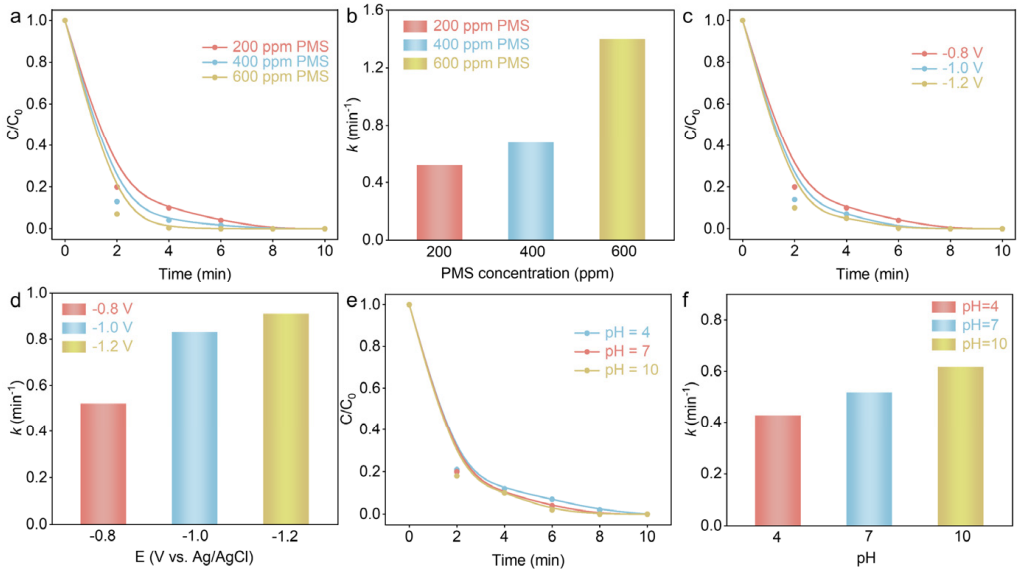

Figure 3. The degradation efficiency and kinetics of PFX in the $Co(OH)_2$@Ti/EA-PMS process under different operating parameters. The effect of PMS concentrations on PFX degradation: (**a**) efficiency and (**b**) kinetics. The effect of voltage on PFX degradation: (**c**) efficiency and (**d**) kinetics. The effect of pH on PFX degradation: (**e**) efficiency and (**f**) kinetics.

3.3. The Mechanism of PFX Degradation in Co(OH)$_2$@Ti/EA-PMS Process

Free radicals generated by PMS electroactivation play a crucial role in the degradation of PFX. Quenching experiments with scavengers were further conducted to clarify the contribution of different free radicals to the degradation of PFX. Meanwhile, furfuryl alcohol (FFA), tert-butanol (TBA), and superoxide dismutase (SOD) were used as the quenching agents for $^1O_2$, •OH, and •O^{2-}, respectively [32,33], and MeOH was used as the quenching agent for •OH and $SO_4^{\bullet-}$ [34]. Employing pseudo-first-order reaction kinetics, the addition of TBA, MeOH, FFA, and SOD resulted in a reduction in the degradation rate constant of PFX by 13.5%, 6.9%, 75.2%, and 7.7%, respectively (Figure 4a,b). Therefore, we concluded that $^1O_2$ was involved in PFX degradation as the main ROS produced by PMS activation. Additionally, we found that the degradation rate of PFX was higher in D_2O compared to H_2O due to the longer lifetime of $^1O_2$ in D_2O, which confirmed that that $^1O_2$ is the main reactive oxygen species involved in PFX degradation (Figure S4) [35]. The DMPO and TEMP spin-trapping ESR was further used to determine the radical species involved in the Co(OH)$_2$@Ti/EA-PMS process [36]. As shown in Figure 4c,d, the signals of $SO_4^{\bullet-}$, •OH, and $^1O_2$ were detected; however, the signal of •O^{2-} was not observed due to the extremely small reaction rate of DMPO with •O^{2-} and the short lifetime of DMPO-•O^{2-} (Figure 4e). In addition, the quantitative analysis of $^1O_2$, $SO_4^{\bullet-}$, •OH, and •O^{2-} radicals produced in the Co(OH)$_2$@Ti/EA-PMS system was performed by the free radical molecular probe method using DPBF (1,3-Diphenylisobenzofuran), p-HBA (4-Hydroxybenzoic acid), TA-PL (terephthalic acid photoluminescence), and NBT (Nitro blue tetrazolium chloride), respectively [37–40]. As shown in Figure 4f, the contribution of the $^1O_2$, $SO_4^{\bullet-}$, •OH, and •O_2^- radicals to PFX degradation was 74.26%, 5.6%, 12.14%, and 8%, respectively, which was consistent with the free radical quenching experiments. The source of ROS was further determined by excluding PMS and O_2 interference separately. As shown in Figure S5, the ROS were mainly derived from PMS activation, and different atmospheres had little effect.

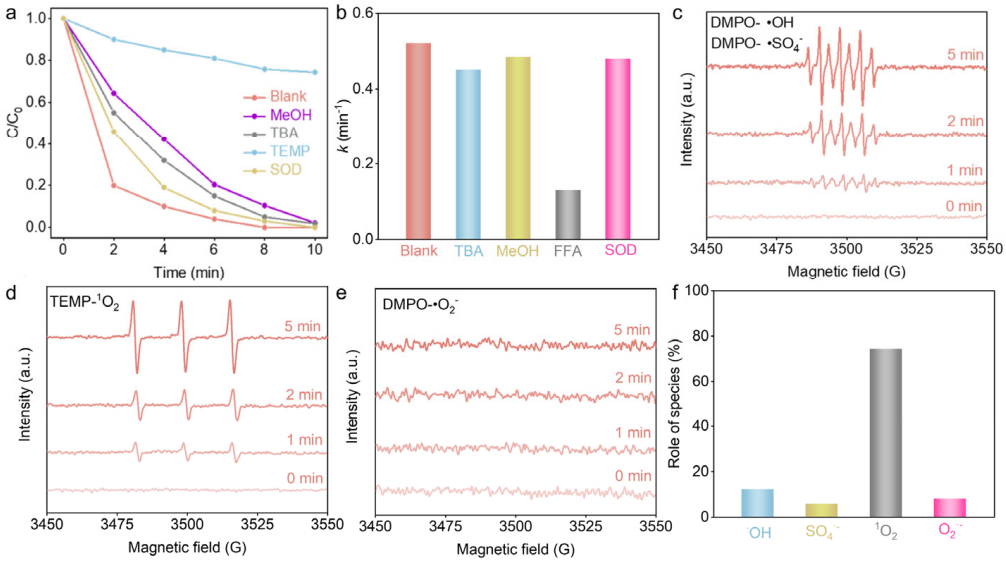

Figure 4. Mechanism of PFX degradation in Co(OH)$_2$@Ti/EA-PMS system. (**a**) PFX degradation curves and (**b**) kinetics with addition of different quenching agents. EPR spectra of (**c**) DMPO-•OH and DMPO-$SO_4^{\bullet-}$, (**d**) TEMP-$^1O_2$, and (**e**) DMPO-•O_2^- in Co(OH)$_2$@Ti/EA-PMS process. (**f**) Proportion of four oxygen species in Co(OH)$_2$@Ti/EA-PMS system.

To clarify the electroactivation mechanism of PMS by Co(OH)$_2$@Ti, XPS was employed to analyze the catalyst chemical valence before and after the reaction. As shown in Figure 5a, the peaks at the binding energies of 781.6 eV and 797.8 eV are assigned to Co^{2+} 2p3/2 and Co^{2+} 2p1/2, respectively [41]. The peaks of Co 2p in Co(OH)$_2$ exhibit a negative shift

of 0.5 eV after the activation process of PMS compared to the initial $Co(OH)_2$. The Co 2p spectra exhibit new peaks corresponding to Co^{3+}, which indicates that the electron transfer resulting from the conversion from Co^{2+} to Co^{3+} was essential for the activation of PMS [42,43]. As shown in Figure 5b, the three characteristic peaks at 531.0 eV, 531.8 eV, and 532.8 eV in the O 1s spectrum are assigned to lattice oxygen, reactive oxygen, and H_2O, respectively [44,45]. The ratio of reactive oxygen/lattice oxygen increases significantly from 1.33 to 2.2 after the PMS activation process, indicating the formation of substantial ROS during the activation of PMS [46,47].

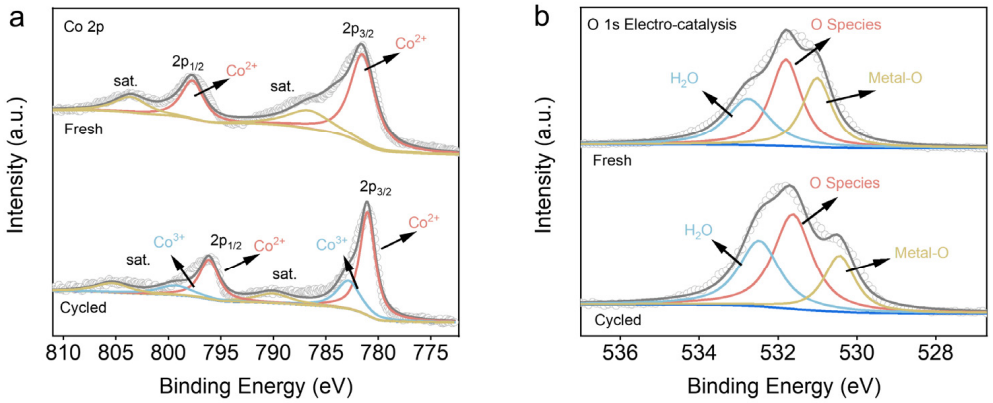

Figure 5. XPS spectrum of $Co(OH)_2$@Ti nanoarray electrodes: (**a**) Co 2p and (**b**) O 1s before (up) and after (down) $Co(OH)_2$@Ti/EA-PMS process.

Based on the above results and previous works, the PFX degradation mechanism in the $Co(OH)_2$@Ti/EA-PMS system was proposed as follows [11,18,48,49]: Firstly, the hydroxyl group on the surface of Co^{2+} is displaced by the $SO_5^{\bullet-}$ group, forming complexes. Subsequently, an internal nucleophilic attack leads to the formation of the intermediate Co^{2+}-OO-Co^{2+} with Co^{2+} on adjacent surfaces, and O-O bond cleavage leads to Co^{3+}, which is similarly stripped of the hydroxyl group on the surface to be replaced by the $SO_5^{\bullet-}$ group, forming the intermediate Co^{3+}-OO-Co^{3+}. Finally, O-O bond cleavage leads to the formation of $^1O_2$ and the regeneration of the active sites. The relevant reactions are represented by Equations (5)–(10):

$$Co^{2+}\text{-}OH + HSO_5^- \rightarrow Co^{2+}\text{-}SO_5^- + H_2O \quad (6)$$

$$Co^{2+}\text{-}SO_5^- + Co^{2+}\text{-}OH \rightarrow Co^{2+}\text{-}OO\text{-}Co^{2+} + H^+ + SO_4^{2-} \quad (7)$$

$$Co^{2+}\text{-}OO\text{-}Co^{2+} + 2H_2O \rightarrow 2Co^{3+}\text{-}OH + 2HO^- \quad (8)$$

$$Co^{3+}\text{-}OH + HSO_5^- \rightarrow Co^{3+}\text{-}SO_5^- + H_2O \quad (9)$$

$$Co^{3+}\text{-}OH + Co^{3+}\text{-}SO_5^- \rightarrow Co^{3+}\text{-}OO\text{-}Co^{3+} + H^+ + SO_4^{2-} \quad (10)$$

$$Co^{3+}\text{-}OO\text{-}Co^{3+} + 2H_2O \rightarrow 2Co^{2+}\text{-}OH + 2H^+ + {}^1O_2 \quad (11)$$

Consequently, we propose that the $Co(OH)_2$@Ti/EA-PMS system could be extended to the treatment of other organic pollutants in wastewater. Using rhodamine B (RhB) and tetracycline (TC) as examples, we found that the degradation efficiency of RhB and TC was almost 100% in the $Co(OH)_2$@Ti/EA-PMS process within 10 min (Figure 6a), and the mineralization rates were 27% and 14% for RhB and TC, respectively (Figure 6b). This result displays the potential practical applications of the $Co(OH)_2$@Ti/EA-PMS process for treating various organic pollutants in wastewater.

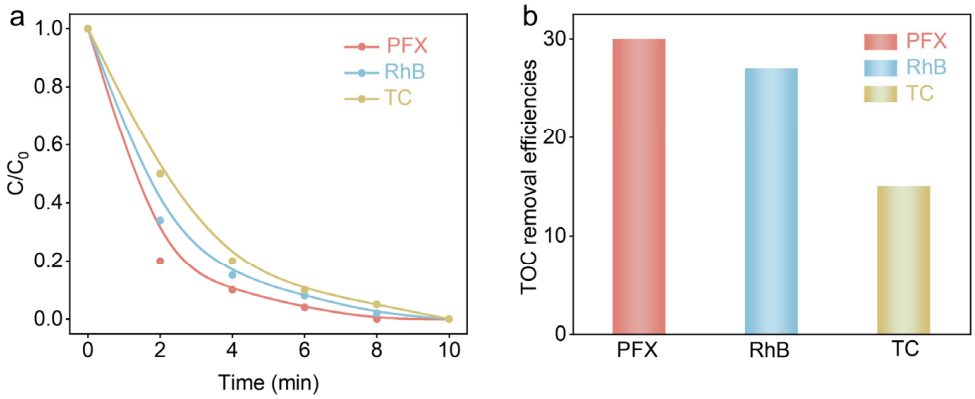

Figure 6. Other organic pollutants' (**a**) degradation curves and (**b**) mineralization rates via $Co(OH)_2$@Ti/EA-PMS process.

4. Conclusions

In this study, $Co(OH)_2$@Ti nanoarray electrodes were successfully fabricated by electrochemical in situ deposition. The catalysts were further characterized by XRD, Raman spectroscopy, SEM, TEM, and XPS to verify the petal-like structure of the $Co(OH)_2$ uniformly loaded on the Ti mesh. In addition, the $Co(OH)_2$@Ti electrode showed an inspiring potential for the removal of PFX by activating PMS, achieving 100% removal of PFX within 10 min at −0.8 V (V vs. Ag/AgCl). Combined with EPR and quenching experiments, we inferred that the PMS activation was mainly due to the electron transfer by redox processes of Co^{2+} and Co^{3+} in the $Co(OH)_2$ catalysts, in which $^1O_2$ was the main active species. On this basis, the PFX degradation mechanism in the $Co(OH)_2$@Ti/EA-PMS system was further proposed. In a word, this work provides an efficient strategy for PFX degradation, and the prepared $Co(OH)_2$@Ti nanoarray electrodes show remarkable stability and performance in activating PMS for the degradation of PFX.

Supplementary Materials: The following supporting information can be downloaded at https://www.mdpi.com/article/10.3390/nano14151312/s1, Table S1: Chemicals and materials; Table S2: Comparison of catalytic performance with other systems; Figure S1: The standard curves of PFX, RhB, and TC. Figure S2: Structural characterization and electrochemical performance of $Co(OH)_2$ catalysts. (a) XPS spectrum and (b) Raman image of $Co(OH)_2$ catalysts. Figure S3: Activating PMS on $Co(OH)_2$ nanoarray electrode. (a) Standard curve of PMS. (b) Degradation curve of PMS. Figure S4: Degradation of PFX under H_2O and D_2O solutions: (a) degradation curves; (b) degradation kinetics. Figure S5: Degradation of PFX under different conditions: (a) degradation curves; (b) degradation kinetics. (References [50–53] are cited in Supplementary Materials).

Author Contributions: Conceptualization, Y.H.; methodology, T.B. and H.K.; formal analysis, T.B. and H.K.; investigation, T.B. and H.K.; data curation, W.L.; writing—original draft preparation, T.B.; writing—review and editing, Y.H. and L.C.; supervision, Y.H.; project administration, Y.H.; funding acquisition, Y.H. All authors have read and agreed to the published version of the manuscript.

Funding: This study was funded by the National Natural Science Foundation of China (U21A20286 and 22206054) and the Hubei Province Natural Science Foundation (2021CFB094).

Data Availability Statement: The data are contained within the article and Supplementary Materials.

Conflicts of Interest: The authors declare no conflicts of interest.

References

1. Yao, B.; Zeng, W.; Núñez-Delgado, A.; Zhou, Y. Simultaneous adsorption of ciprofloxacin and Cu^{2+} using Fe and N co-doped biochar: Competition and selective separation. *Waste Manag.* **2023**, *168*, 386–395. [CrossRef]
2. Zhang, Y.; Hu, Y.; Li, X.; Gao, L.; Wang, S.; Jia, S.; Shi, P.; Li, A. Prevalence of antibiotics, antibiotic resistance genes, and their associations in municipal wastewater treatment plants along the Yangtze River basin, China. *Environ. Pollut.* **2024**, *348*, 123800. [CrossRef]

3. Zhou, Y.; Wang, J. Electro-Fenton degradation of pefloxacin using MOFs derived Cu, N co-doped carbon as a nanocomposite catalyst. *Environ. Pollut.* **2024**, *355*, 124198. [CrossRef]
4. Liu, D.; Xue, X.; Zhang, X.; Huang, Y.; Feng, P. Highly efficient peroxymonosulfate activation by MOFs-derived oxygen vacancy-rich Co_3O_4/ZnO p-n heterojunction nanocomposites to degrade pefloxacin. *Sep. Purif. Technol.* **2023**, *305*, 122451. [CrossRef]
5. Li, M.; Jia, L.; Chen, X.; Li, Y.; Zhao, D.; Zhang, L.; Zhao, T.; Xu, J. Web system-assisted ratiometric fluorescent probe embedded with machine learning for intelligent detection of pefloxacin. *Sens. Actuators B Chem.* **2024**, *407*, 135491. [CrossRef]
6. Wang, J.; Chu, L.; Wojnárovits, L.; Takács, E. Occurrence and fate of antibiotics, antibiotic resistant genes (ARGs) and antibiotic resistant bacteria (ARB) in municipal wastewater treatment plant: An overview. *Sci. Total Environ.* **2020**, *744*, 140997. [CrossRef]
7. Yao, B.; Qin, T.; Zhao, C.; Zhou, Y. Degradation of sulfanilamide in aqueous solution by ionizing radiation: Performance and mechanism. *Environ. Pollut.* **2023**, *338*, 122681. [CrossRef]
8. Huang, X.; Wen, D.; Wang, J. Radiation-induced degradation of sulfonamide and quinolone antibiotics: A brief review. *Radiat. Phys. Chem.* **2024**, *215*, 111373. [CrossRef]
9. Zhuang, S.; Wang, J. Adsorptive removal of pharmaceutical pollutants by defective metal organic framework UiO-66: Insight into the contribution of defects. *Chemosphere* **2021**, *281*, 130997. [CrossRef]
10. Ghanbari, F.; Moradi, M. Application of peroxymonosulfate and its activation methods for degradation of environmental organic pollutants: Review. *Chem. Eng. J.* **2017**, *310*, 41–62. [CrossRef]
11. Oh, W.-D.; Dong, Z.; Lim, T.-T. Generation of sulfate radical through heterogeneous catalysis for organic contaminants removal: Current development, challenges and prospects. *Appl. Catal. B* **2016**, *194*, 169–201. [CrossRef]
12. Abdelrahman, A.; Ganiyu, S.O.; Gamal El-Din, M. Degradation of surrogate and real naphthenic acids from simulated and real oil sands process water using electrochemically activated peroxymonosulfate (EO-PMS) process. *Sep. Purif. Technol.* **2023**, *306*, 122462. [CrossRef]
13. Li, S.; Zhou, M.; Wu, H.; Song, G.; Jing, J.; Meng, N.; Wang, W. High-efficiency degradation of carbamazepine by the synergistic electro-activation and bimetals (FeCo@NC) catalytic-activation of peroxymonosulfate. *Appl. Catal. B* **2023**, *338*, 123064. [CrossRef]
14. Yu, S.; Zhang, Q.; Sun, X.; Chen, S.; Tang, J.; Zhu, J.-J.; Dang, Y. Doping Sb into $CuFe_2O_4$ improved the catalytic performance in the electrochemically enhanced homogeneous peroxymonosulfate-heterogeneous catalytic system for the degradation of ciprofloxacin. *J. Environ. Chem. Eng.* **2022**, *10*, 108335. [CrossRef]
15. Wang, H.; Liu, H.; Chu, Z.; Sun, F.; Zou, X.; Wang, Q.; Chen, T.; Chen, D.; Wang, H. Fe_3O_4 derived from the decomposition of siderite as a heterogeneous photocatalyst to degrade 2,4-dichlorophenol via activating PMS. *J. Water Process Eng.* **2024**, *57*, 104538. [CrossRef]
16. Li, J.; Xu, M.; Yao, G.; Lai, B. Enhancement of the degradation of atrazine through $CoFe_2O_4$ activated peroxymonosulfate (PMS) process: Kinetic, degradation intermediates, and toxicity evaluation. *Chem. Eng. J.* **2018**, *348*, 1012–1024. [CrossRef]
17. Gerken, J.B.; McAlpin, J.G.; Chen, J.Y.C.; Rigsby, M.L.; Casey, W.H.; Britt, R.D.; Stahl, S.S. Electrochemical Water Oxidation with Cobalt-Based Electrocatalysts from pH 0–14: The Thermodynamic Basis for Catalyst Structure, Stability, and Activity. *J. Am. Chem. Soc.* **2011**, *133*, 14431–14442. [CrossRef]
18. Li, B.; Wang, Y.-F.; Zhang, L.; Xu, H.-Y. Enhancement strategies for efficient activation of persulfate by heterogeneous cobalt-containing catalysts: A review. *Chemosphere* **2022**, *291*, 132954. [CrossRef]
19. Wang, J.; Wang, S. Activation of persulfate (PS) and peroxymonosulfate (PMS) and application for the degradation of emerging contaminants. *Chem. Eng. J.* **2018**, *334*, 1502–1517. [CrossRef]
20. Quan, X.; Zhang, J.; Yin, L.; Zuo, W.; Tian, Y. Fe_3O_4 decorated with α-cyclodextrin for enhanced peroxymonosulfate(PMS)-activated degradation of PPCPs. *Sep. Purif. Technol.* **2023**, *317*, 123904. [CrossRef]
21. Zhou, Z.; Liu, T.; Wu, J.; Li, H.; Chu, S.; Zhu, X.; Zhang, L.; Lu, J.; Ivanets, A.; Davronbek, B.; et al. Preparation of copper-based catalysts from electroplating sludge by ultrasound treatment and their antibiotic degradation performance. *Environ. Res.* **2023**, *216*, 114567. [CrossRef] [PubMed]
22. Chen, L.; Ding, D.; Liu, C.; Cai, H.; Qu, Y.; Yang, S.; Gao, Y.; Cai, T. Degradation of norfloxacin by $CoFe_2O_4$-GO composite coupled with peroxymonosulfate: A comparative study and mechanistic consideration. *Chem. Eng. J.* **2018**, *334*, 273–284. [CrossRef]
23. Dong, P.; Chen, X.; Guo, M.; Wu, Z.; Wang, H.; Lin, F.; Zhang, J.; Wang, S.; Zhao, C.; Sun, H. Heterogeneous electro-Fenton catalysis with self-supporting CFP@MnO_2-Fe_3O_4/C cathode for shale gas fracturing flowback wastewater. *J. Hazard. Mater.* **2021**, *412*, 125208. [CrossRef]
24. Yu, F.; Guo, Y.; Li, H.; Yang, J. Activated persulfate by the synergistic electro-activation and bimetals cathode (MBC@CF) leads to highly efficient degradation of tetracycline. *Sep. Purif. Technol.* **2024**, *335*, 126204. [CrossRef]
25. Ganiyu, S.O.; Hussain, N.A.S.; Stafford, J.L.; Gamal El-Din, M. Electrocatalytic activation of peroxomonosulfate (PMS) under aerobic condition for the remediation of oil sands process water: Insight into one-pot synergistic coupling of PMS electro-activation and heterogeneous electro-Fenton processes. *Chem. Eng. J.* **2024**, *480*, 147737. [CrossRef]
26. Yu, C.; Zhao, Z.; Zong, Y.; Xu, L.; Zhang, B.; Wu, D. Electric field-enhanced coupled with metal-free peroxymonosulfate activactor: The selective oxidation of nonradical species-dominated system. *Water Res.* **2022**, *227*, 119323. [CrossRef]

27. Di, J.; Zhu, M.; Jamakanga, R.; Gai, X.; Li, Y.; Yang, R. Electrochemical activation combined with advanced oxidation on $NiCo_2O_4$ nanoarray electrode for decomposition of Rhodamine B. *J. Water Process Eng.* **2020**, *37*, 101386. [CrossRef]
28. Zhang, M.; Gong, Y.; Ma, N.; Zhao, X. Promoted photoelectrocatalytic degradation of BPA with peroxymonosulfate on a $MnFe_2O_4$ modified carbon paper cathode. *Chem. Eng. J.* **2020**, *399*, 125088. [CrossRef]
29. Lv, S.; Xia, G.; Jin, C.; Hao, C.; Wang, L.; Li, J.; Zhang, Y.; Zhu, J.J. Low-temperature CO oxidation by Co_3O_4 nanocubes on the surface of Co(OH)2 nanosheets. *Catal. Commun.* **2016**, *86*, 100–103. [CrossRef]
30. Xie, D.; Chu, S.; Zhang, S.; Ivanets, A.; Zhang, L.; Su, X. Facile synthesis of Cr-doped ferrite catalyst from Cr-containing electroplating sludge with activated persulfate for efficient degradation of tetracycline. *J. Environ. Chem. Eng.* **2022**, *10*, 108805. [CrossRef]
31. Zhou, Z.; Zhang, L.; Yan, B.; Wu, J.; Kong, D.; Romanovski, V.; Ivanets, A.; Li, H.; Chu, S.; Su, X. Removal of chromium from electroplating sludge by roasting-acid leaching and catalytic degradation of antibiotics by its residue. *J. Environ. Chem. Eng.* **2024**, *12*, 111754. [CrossRef]
32. Cheng, X.; Guo, H.; Zhang, Y.; Wu, X.; Liu, Y. Non-photochemical production of singlet oxygen via activation of persulfate by carbon nanotubes. *Water Res.* **2017**, *113*, 80–88. [CrossRef] [PubMed]
33. Borgstahl, G.E.O.; Oberley-Deegan, R.E. Superoxide Dismutases (SODs) and SOD Mimetics. *Antioxidants* **2018**, *7*, 156. [CrossRef] [PubMed]
34. Tan, C.; Gao, N.; Deng, Y.; Deng, J.; Zhou, S.; Li, J.; Xin, X. Radical induced degradation of acetaminophen with Fe_3O_4 magnetic nanoparticles as heterogeneous activator of peroxymonosulfate. *J. Hazard. Mater.* **2014**, *276*, 452–460. [CrossRef] [PubMed]
35. Lang, Y.; Wu, S.; Yang, Q.; Luo, Y.; Jiang, X.; Wu, P. Analysis of the Isotopic Purity of D_2O with the Characteristic NIR-II Phosphorescence of Singlet Oxygen from a Photostable Polythiophene Photosensitizer. *Anal. Chem.* **2021**, *93*, 9737–9743. [CrossRef] [PubMed]
36. Guan, C.; Jiang, J.; Pang, S.; Chen, X.; Webster, R.D.; Lim, T.-T. Facile synthesis of pure g-C_3N_4 materials for peroxymonosulfate activation to degrade bisphenol A: Effects of precursors and annealing ambience on catalytic oxidation. *Chem. Eng. J.* **2020**, *387*, 123726. [CrossRef]
37. Żamojć, K.; Zdrowowicz, M.; Rudnicki-Velasquez, P.B.; Krzymiński, K.; Zaborowski, B.; Niedziałkowski, P.; Jacewicz, D.; Chmurzyński, L. The development of 1,3-diphenylisobenzofuran as a highly selective probe for the detection and quantitative determination of hydrogen peroxide. *Free Radic. Res.* **2017**, *51*, 38–46. [CrossRef] [PubMed]
38. Joo, S.H.; Feitz, A.J.; Sedlak, D.L.; Waite, T.D. Quantification of the Oxidizing Capacity of Nanoparticulate Zero-Valent Iron. *Environ. Sci. Technol.* **2005**, *39*, 1263–1268. [CrossRef] [PubMed]
39. Žerjav, G.; Albreht, A.; Vovk, I.; Pintar, A. Revisiting terephthalic acid and coumarin as probes for photoluminescent determination of hydroxyl radical formation rate in heterogeneous photocatalysis. *Appl. Catal. A* **2020**, *598*, 117566. [CrossRef]
40. Fu, Y.; Li, Z.; Liu, Q.; Yang, X.; Tang, H. Construction of carbon nitride and MoS_2 quantum dot 2D/0D hybrid photocatalyst: Direct Z-scheme mechanism for improved photocatalytic activity. *Chin. J. Catal.* **2017**, *38*, 2160–2170. [CrossRef]
41. Li, K.; Zhao, B.; Bai, J.; Ma, H.; Fang, Z.; Zhu, X.; Sun, Y. A High-Energy-Density Hybrid Supercapacitor with P-$Ni(OH)_2$@$Co(OH)_2$ Core–Shell Heterostructure and Fe_2O_3 Nanoneedle Arrays as Advanced Integrated Electrodes. *Small* **2020**, *16*, 2001974. [CrossRef] [PubMed]
42. Wang, J.; Gao, R.; Zhou, D.; Chen, Z.; Wu, Z.; Schumacher, G.; Hu, Z.; Liu, X. Boosting the Electrocatalytic Activity of Co_3O_4 Nanosheets for a Li-O_2 Battery through Modulating Inner Oxygen Vacancy and Exterior Co^{3+}/Co^{2+} Ratio. *ACS Catal.* **2017**, *7*, 6533–6541. [CrossRef]
43. Zhao, P.; Fu, S.; Luo, Y.; Peng, C.; Cheng, L.; Jiao, Z. Deciphering the Space Charge Effect of the CoNiLDH/FeOOH n–n Heterojunction for Efficient Electrocatalytic Oxygen Evolution. *Small* **2023**, *19*, 2305241. [CrossRef]
44. Lan, D.; Gao, Z.; Zhao, Z.; Wu, G.; Kou, K.; Wu, H. Double-shell hollow glass microspheres@Co_2SiO_4 for lightweight and efficient electromagnetic wave absorption. *Chem. Eng. J.* **2021**, *408*, 127313. [CrossRef]
45. Zhang, Y.; Hu, Y.; Wang, Z.; Lin, T.; Zhu, X.; Luo, B.; Hu, H.; Xing, W.; Yan, Z.; Wang, L. Lithiation-Induced Vacancy Engineering of Co_3O_4 with Improved Faradic Reactivity for High-Performance Supercapacitor. *Adv. Funct. Mater.* **2020**, *30*, 2004172. [CrossRef]
46. Yan, M.; Zhao, Z.; Cui, P.; Mao, K.; Chen, C.; Wang, X.; Wu, Q.; Yang, H.; Yang, L.; Hu, Z. Construction of hierarchical $FeNi_3$@(Fe,Ni)S_2 core-shell heterojunctions for advanced oxygen evolution. *Nano Res.* **2021**, *14*, 4220–4226. [CrossRef]
47. Yan, M.; Mao, K.; Cui, P.; Chen, C.; Zhao, J.; Wang, X.; Yang, L.; Yang, H.; Wu, Q.; Hu, Z. In situ construction of porous hierarchical (Ni_3-xFex)FeN/Ni heterojunctions toward efficient electrocatalytic oxygen evolution. *Nano Res.* **2020**, *13*, 328–334. [CrossRef]
48. Zhang, Z.; Zhan, X.; Hong, B.; Wang, X.; Tang, P.; Ding, Y.; Xia, Y.; Zeng, Y. Edge interface microenvironment regulation of CoOOH/commercial activated carbon nano-hybrids enabling PMS activation for degrading ciprofloxacin. *J. Colloid Interface Sci.* **2024**, *663*, 909–918. [CrossRef] [PubMed]
49. Dong, S.; Yang, S.; Chen, Y.; Kuss, C.; Cui, G.; Johnson, L.R.; Gao, X.; Bruce, P.G. Singlet oxygen and dioxygen bond cleavage in the aprotic lithium-oxygen battery. *Joule* **2022**, *6*, 185–192. [CrossRef]
50. Li, W.; Li, W.; He, K.; Tang, L.; Liu, Q.; Yang, K.; Chen, Y.-D.; Zhao, X.; Wang, K.; Lin, H.; et al. Peroxymonosulfate activation by oxygen vacancies-enriched MXene nano-Co3O4 co-catalyst for efficient degradation of refractory organic matter: Efficiency, mechanism, and stability. *J. Hazard. Mater.* **2022**, *432*, 128719. [CrossRef]

51. Xu, P.; Wang, P.; Li, X.; Wei, R.; Wang, X.; Yang, C.; Shen, T.; Zheng, T.; Zhang, G. Efficient peroxymonosulfate activation by CuO-Fe_2O_3/MXene composite for atrazine degradation: Performance, coexisting matter influence and mechanism. *Chem. Eng. J.* **2022**, *440*, 135863. [CrossRef]
52. Song, H.; Du, R.; Wang, Y.; Zu, D.; Zhou, R.; Cai, Y.; Wang, F.; Li, Z.; Shen, Y.; Li, C. Anchoring single atom cobalt on two-dimensional MXene for activation of peroxymonosulfate. *Appl. Catal. B* **2021**, *286*, 119898. [CrossRef]
53. Guo, L.; Zhao, J.; Zhao, L.; Tang, Y.; Zhou, J.; Shi, B. Persulfate activation by Cr2O3/BC derived from chrome shavings for antibiotics degradation. *Chem. Eng. J.* **2021**, *420*, 127698. [CrossRef]